

## DUST AND GAS IN NGC3627



DUST AND GAS IN NGC3627 USING OBSERVATIONS FROM  
SCUBA-2

By

JONATHAN H. NEWTON, B.A.

A Thesis

Submitted to the School of Graduate Studies

in Partial Fulfilment of the Requirements

for the Degree

Master of Science

McMaster University

©Copyright by Jonathan Newton, August 2014

MASTER OF SCIENCE (2014)

McMaster University

(Physics and Astronomy)

Hamilton, Ontario

TITLE: Dust and Gas in NGC3627 Using Observations from SCUBA-2

AUTHOR: Jonathan Newton, B.A. (Western Kentucky University)

SUPERVISOR: Christine D. Wilson

NUMBER OF PAGES: ix, 43

# Abstract

Saw some dust and wanted to do something about it!

*To my family and Poly.*

# Acknowledgements

*When life looks like easy street, there is danger at your door... -Robert Hunter*

Thank Chris and group members of course. Don't forget Christian!

# Table of Contents

<b>Descriptive Notes</b>	ii
<b>Abstract</b>	iii
<b>Acknowledgements</b>	v
<b>List of Figures</b>	viii
<b>List of Tables</b>	ix
 <b>Chapter 1 Introduction</b>	 <b>1</b>
1.1 The Physical Conditions of Star Formation . . . . .	1
1.2 Determining H <sub>2</sub> Abundance . . . . .	7
 <b>Chapter 2 Observations and Data Preparation</b>	 <b>8</b>
2.1 SCUBA-2 . . . . .	8
2.2 Image Creation and Properties . . . . .	9
2.2.1 Beam Shape of the 450 $\mu$ m and 850 $\mu$ m Data . . . . .	17
2.3 Ancillary Data . . . . .	17
2.3.1 Key Insights on Nearby Galaxies: a Far-Infrared Survey with Herschel (KINGFISH) . . . . .	19
2.3.2 Nearby Galaxy Legacy Survey (NGLS) . . . . .	20
2.3.3 Nobeyama 45-m . . . . .	27



2.3.4	Hetrodyne Reciever Array CO-Line Extragalactic Survey (HERACLES) . . . . .	27
2.3.5	The HI Nearby Galaxy Survey (THINGS) . . . . .	29
2.4	Data Preparation for Analysis . . . . .	31
2.4.1	Accounting for the $450\mu\text{m}$ Error Beam . . . . .	33
2.4.2	Extended Structure Removal via MAKEMAP . . . . .	34
<b>Chapter 3</b>	<b>Results</b>	<b>37</b>
3.1	Will they ever get here? . . . . .	37
<b>Chapter 4</b>	<b>Discussion</b>	<b>38</b>
4.1	Talk to the hand . . . . .	38
<b>Chapter 5</b>	<b>Conclusions</b>	<b>39</b>

# List of Figures

2.1	Flux Values vs High-Pass Filter Sizes . . . . .	12
2.2	450 $\mu$ m High-Pass Filter Images . . . . .	13
2.3	850 $\mu$ m High-Pass Filter Images . . . . .	14
2.4	NGC3627 450 $\mu$ m Observations . . . . .	15
2.5	NGC3627 850 $\mu$ m Observations . . . . .	16
2.6	SCUBA-2 Calibration and Beams . . . . .	18
2.7	NGC3627 100 $\mu$ m Observations . . . . .	21
2.8	NGC3627 160 $\mu$ m Observations . . . . .	22
2.9	NGC3627 250 $\mu$ m Observations . . . . .	23
2.10	NGC3627 350 $\mu$ m Observations . . . . .	24
2.11	NGC3627 500 $\mu$ m Observations . . . . .	25
2.12	NGC3627 CO j=3-2 Observations . . . . .	26
2.13	NGC3627 CO j=1-0 Observations . . . . .	28
2.14	NGC3627 CO j=2-1 Observations . . . . .	30
2.15	NGC3627 HI Observations . . . . .	32

# List of Tables

2.1	Properties of NGC3627 SCUBA-2 Observations . . . . .	12
2.2	Properties of NGC3627 KINGFISH Observations . . . . .	20
2.3	Properties of NGC3627 NGLS Observations . . . . .	21
2.4	Properties of NGC3627 Nobeyama 45-m Observations . . . . .	27
2.5	Properties of NGC3627 HERACLES Observations . . . . .	29
2.6	Properties of NGC3627 THINGS Observations . . . . .	31



# Chapter 1

## Introduction

### 1.1 The Physical Conditions of Star Formation

Star formation is one of the fundamental processes in astrophysics that effect not just stellar and planetary formation but also dictate behavior in galaxy formation and evolution (Kennicutt & Evans, 2012). The study of star formation itself can be broken into several areas such as: the processes that trigger collapse and how the collapse behaves, dictating how and what type of stars can form from a given region or cloud, or how the inflow of new material can alter current star forming environments. These different sub-branches of star formation are conveniently sorted into a hierarchical schemes that range from Mpc scales seen in gas accretion from the intergalactic medium, to small scale effects on the order  $R_{\odot}$  or AU (Kennicutt & Evans, 2012).

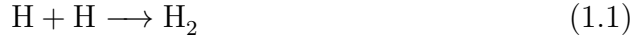
After the intergalactic gas has accreted into a host galaxy, it will eventually condense and begin to form a giant molecular cloud (GMC). The formation of molecular clouds has divided between two camps; either a “bottom-up” or

“top-down” formation (McKee & Ostriker, 2007). The bottom-up scenario consists of small clouds of cold HI coagulating to eventually form a GMC (Field & Saslaw, 1965; Kwan, 1979). The major concern with the bottom-up scenario is the time scales required to form a cloud typical of what we observe. The time scale required would take around  $10^8$  years which is longer than the expected GMC lifetime (McKee & Ostriker, 2007).

The alternative formation scenario, top-down, postulates the GMC formation comes from instabilities in diffuse ISM causing the clouds to collapse from their surrounding medium (McKee & Ostriker, 2007). Two main instabilities are thought to be responsible for the collapse. The first type of instability is the Parker instability, which involves distortion of magnetic fields in the mid plane of the galaxy, and at these distortions gas will begin to accumulate (Parker, 1966; Dobbs et al., 2013). The second instability responsible for collapse comes in the style of a more complex Jeans instability which is determined further by the amount of rotational shear present (McKee & Ostriker, 2007). If a strong rotational shear is present, such as in the inter arm region of a spiral galaxy, then a process known as swing amplification will occur (McKee & Ostriker, 2007). If no rotational shear is present, such as the inner regions of a galaxy or spiral arms, then the collapse can be attributed to a magneto-Jeans instability (Elmegreen, 1987; Kim & Ostriker, 2001).

During the collapse or coagulation of a GMC, molecular hydrogen is being formed inside of the cloud. The formation of molecular hydrogen can be summarized using either the two bodied reaction, three bodied reaction, formation using free a electron or proton, or surface formation (Krumholz, 2014). The

two bodied formation scenario is the simplest reaction using two hydrogen atoms to molecular hydrogen, reaction 1.1.



However the two bodied formation is not the major mechanism in the formation of  $\text{H}_2$  due to the requirement of a forbidden photon that arises from the combination of hydrogen atoms in the ground state (Gould & Salpeter, 1963). If one of the hydrogen atoms is excited, the transition can occur, but the amount of excited hydrogen atoms in the temperature ranges typical of the cold and warm phases of the ISM are expected to be nearly nonexistent (Krumholz, 2014).

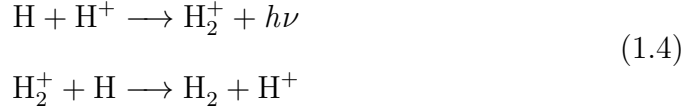
The second formation scenario listed, the three bodied formation, involves three hydrogen atoms coming together to form molecular hydrogen with a spare hydrogen atom shown in reaction 1.2.



The three bodied formation scenario however is not expected to be the dominant form of  $\text{H}_2$  formation due to the required density of  $10^8 \text{ cm}^{-3}$  (Palla et al., 1983; Abel et al., 1997), while the normal density of a GMC is on the order of  $300 \text{ cm}^{-3}$  (Krumholz, 2014).

An alternative to the two or three bodied reactions uses either an electron or proton to ionize the hydrogen forming either  $\text{H}^-$  or  $\text{H}_2^+$  (Krumholz, 2014). The

chemical reaction involving an electron is shown in reaction 1.3 and reaction utilizing a proton is shown in reaction 1.3



The main limitation of the free electron/proton formation mechanism is an undersupply of free electrons and protons. Typical Milky Way conditions show that in regions  $>1 \text{ cm}^{-3}$  have free electron and proton densities  $<10^{-4} \text{ cm}^{-3}$  (Wolfire et al., 2003). Secondly, the  $\text{H}^-$  ion in reaction 1.3 is more likely to interact with a stray photon rather than an electron resulting in ion to return to the atomic state (Glover, 2003). While we observe singly ionized hydrogen regions, HII regions, only a small fraction of the region will successfully produce molecular hydrogen.

While the free electron/proton formation method is suspected to be the primary  $\text{H}_2$  catalyst in the early universe (Herbst et al., 2005), at low redshifts the formation of molecular hydrogen on the surface of dust grains is the dominant mechanism of formation (Krumholz, 2014). The surface formation of molecular hydrogen will occur when a hydrogen atom strikes a dust grain and successfully sticks to the grain. The hydrogen then will then interact with another hydrogen atom to form  $\text{H}_2$  and be ejected off of the dust particle after the reaction has occurred (Pirronello et al., 1997). The same process occurs on the dust grain as the two bodied formation, but the dust grain will act



as a medium to absorb the energy that would create the forbidden photon (Krumholz, 2014).

With a dominant mechanism for molecular hydrogen formation, a reaction rate can be defined based on the cross section of the grain,  $\Sigma_{gr}$ , a striking probability dependent on the temperature of the observed dust,  $S(T)$ , the probability of molecular hydrogen forming on the grain,  $\epsilon_{H_2}$ , density of hydrogen nucleon,  $n_H$ , and the density of free hydrogen in the GMC,  $n_{H_0}$  (Krumholz, 2014). Scaling this with the integrated collisional probability of a Maxwellian gas, a reaction rate is derived and shown in equation 1.5 where  $k$  is the Boltzmann constant,  $T$  is the temperature, and  $m_H$  is the mass of the hydrogen atom.

$$\frac{dn_{H_2}}{dt} = \frac{1}{2} \left( \frac{8k_b T}{\pi m_H} \right)^{\frac{1}{2}} \Sigma_{gr} S(T) \epsilon_{H_2} n_H n_{H_0} \quad (1.5)$$

Equation 1.5 is often simplified to equation 1.6 by introducing a variable known as the formation rate,  $\mathcal{R}_{gr}$  that is constrained using the column densities CI, CII, HI, H<sub>2</sub>, and has been found to be  $3 \times 10^{-17} \text{cm}^3 \text{s}^{-1}$  for the Milky Way (Jura, 1975; Gry et al., 2002; Wolfire et al., 2008).

$$\frac{dn_{H_2}}{dt} = \mathcal{R}_{gr} n_H n_{H_0} \quad (1.6)$$

When the molecular hydrogen has formed, it is still susceptible to photodissociation from far ultra-violet (FUV) photons. The energy required in a single photon to break the bonds of molecular hydrogen is 14.5 eV which conveniently is also enough energy to excite atomic hydrogen, so photodissociation using a single photon is highly unlikely (Krumholz, 2014). However, a photon

with an energy of 11-13.6 eV will not be able to excite atomic hydrogen, but will be able to excite the molecular hydrogen to its first and second excitation levels, the Lyman and Werner bands respectively. The excited  $H_2$  will eventually settle via photon emission to its ground state with a finite probability of returning to two hydrogen atoms rather than maintaining its molecular state (Krumholz, 2014).

A disassociation rate,  $\zeta_{diss}$ , can be obtained by scaling the excitation rate,  $\zeta_{exc}$ , by the fraction of excited hydrogen molecules that will settle to an atomic ground state (Krumholz, 2014). The excitation rate for the Milky Way is found by summing each of the possible excitations. In the Milky Way's diffuse ISM, the interstellar radiation field is  $6-9 \times 10^{-14}$  erg  $cm^{-3}$  over the range of 6-13.6 eV resulting in  $\zeta_{exc} \approx 3 \times 10^{-10} s^{-1}$  (Draine, 2011). The expected fraction of  $H_2$  to disassociate is between 0.11 and 0.13 resulting in  $\zeta_{diss} \approx 4 \times 10^{-11} s^{-1}$  (Draine, 2011). Equating the formation and disassociation rates then solving for a molecular hydrogen vs atomic hydrogen ratio is shown in equation 1.7 (Krumholz, 2014). From equation 1.7 we can see, in the diffuse medium, atomic hydrogen is far more abundant which is of no surprise.

$$\begin{aligned} \frac{n_{H_2}}{n_H} &= \frac{\mathcal{R}n_{H_0}}{\zeta_{diss}} \\ &= 8 \times 10^{-6} \left( \frac{4 \times 10^{-11} s^{-1}}{\zeta_{diss}} \right) \left( \frac{n_{H_0}}{10 cm^{-3}} \right) \end{aligned} \quad (1.7)$$

However, as the density of the gas increases via collapse or coagulation, the optical depth will also increase limiting the amount of FUV photons to penetrate deeply into the cloud; a process known as shielding (Draine, 2011). This shielding will aid in the decrease of  $\zeta_{diss}$  which will increase the value

in equation 1.7. The increase in molecular to atomic hydrogen ratio signifies the accumulation of molecular gas reservoirs. The molecular gas build up will eventually lead to further collapse within the cloud that will eventually lead to forming stars. It is this stage of molecular gas development in star formation that we are examining in this thesis.

## 1.2 Determining H<sub>2</sub> Abundance

## Chapter 2

# Observations and Data Preparation

### 2.1 SCUBA-2

The Submillimetre Common-User Bolometer Array 2 (SCUBA-2) was designed to decrease the observing time of the sub-millimeter sky relative to its predecessor SCUBA (Holland et al., 2013). This would benefit the community by allowing for rapid data acquisition in the submillimeter regime of the electromagnetic spectrum, at the  $450\mu\text{m}$  and  $850\mu\text{m}$  bands in particular. Prior to SCUBA-2, other bolometer camera's such as LABOCA, BOLOCAM and SHARC-II were limited to less than 100 pixels, while the new SCUBA-2 has been able to incorporate over 10,000 pixels in its design and effectively reduce the required observing time (Chapin et al., 2013). Increasing the amount of pixels by a factor of 100 was possible by the advent of new technology such as high precision micromachining, superconducting transition edge sensors, and superconducting quantum interference device amplifiers (SQUIDs) (Holland et al., 2013).

The observations of NGC3627 were taken from the Nearby Galaxies Legacy Survey’s (NGLS) initial science images using SCUBA-2 from December 29, 2011 to January 21, 2012, and consist of 24 18' by 18' scans taken in grade 3 weather or better ( $0.08 < \tau < 0.12$ ) with observations centered at  $450\mu\text{m}$  and  $850\mu\text{m}$  emission with a  $32\mu\text{m}$  and  $85\mu\text{m}$  bandpass respectively. 16 of the 24 scans were deemed useable, and whether or not an observation was deemed worthwhile was determined by factors such as the behavior of the image background or whether the image was flagged during observing to be unusable. The observations of NGC3627 were taken using a daisy scanning pattern to help remove any random noise by introducing crossing points. The scanning speed of the JCMT was  $150''/\text{second}$  in order to negate any drifting effects seen from the instrumentation (Chapin et al., 2013).

## 2.2 Image Creation and Properties

For any imaging process to have be successful, the image need to have limited white noise (Chapin et al., 2013). White noise in the sense of our bolometer observations arise from thermal variations in the instrument and atmosphere during data acquisition. The random noise is minimized through scanning methods and during image processing (Chapin et al., 2013). To create the final SCUBA-2 data products we use the Submillimetre User Reduction Facility (SMURF) procedure MAKEMAP. This procedure reduces the noise of the observations while maintaining the source’s emission by incorporating a combination of principal component analysis and a maximum likelihood analysis (Chapin et al., 2013). Both of these methods have proven useful in

reducing bolometer data on their own, but due to the size of raw SCUBA-2 data, either method on its own would result in extreme run times or the process becoming resource intensive (Chapin et al., 2013).

MAKEMAP breaks down the image creation into several steps performed in iteration in order to successfully reduce any background noise (Chapin et al., 2013). The raw data is approximated by equation 2.1 such that  $b_i(t)$  is the  $i^{th}$  bolometer output at time  $t$ ,  $f$  is a scaling factor determined from flat field calibrations,  $e_i(t)$  is the extinction at time  $t$  for the  $i^{th}$  bolometer,  $a_i(t)$  is the astronomical signal for  $i^{th}$  bolometer at time  $t$ , noise from the product of the common mode and gain,  $g_i * n_c(t)$ , low-frequency noise  $n_f(t)$  and random noise  $n_r(t)$  (Chapin et al., 2013).

$$b_i(t) = f [e_i(t) * a_i(t) + g_i * n_c(t) + n_f(t) + n_r(t)] \quad (2.1)$$

The steps used in MAKEMAP are: COM and GAI which estimate a common mode signal and from the fitting averaging time-series of each bolometer observation, EXT to apply the measured extinction corrections, FLT to apply a high- and low-pass filters to remove any noise features not removed in the COM and GAI filtering, AST which regrids the data and detects sources to be removed from reduction. The final step is NOI which determines the noise in the gridded map after each step has been performed and is calculated by isolating the white noise component in equation 2.1. A convergence check is then issued based on the magnitude of change in each pixel from the previous map and the current version. If the check failed the COM, GAI, EXT, and FLT values are recalculated using the AST information obtained from the pre-

vious iteration, and the process is repeated until the convergene values are met or the maximum number of iterations have been carried out (Chapin et al., 2013).

In our production of maps, we used the configuration file `dimconfig_bright_compact.lis` and altered the AST and FLT sections of the image creation by introducing a mask made from Herschel’s  $250\mu\text{m}$  map. The purpose of the mask was to exclude the target from interfering with the noise minimization as well as prohibit any emission from the galaxy to be significantly altered during image production. The filter size of the high-pass filter was also modified, and an appropriate value was determined to be  $175''$ . We determined an appropriate high-pass filter size by running a large range of filters from  $100''$  to  $300''$  and inspecting the total recovered flux of NGC3627. A plot of the returned flux values can be seen in figure 2.2. An good filter would not show any significant decrease flux compared to the  $350\mu\text{m}$  or  $500\mu\text{m}$ . This requirement removes any filters greater than  $200''$ . Given the flux was nearly unchaning with filters less than  $200''$ , we determiend an appropriate filter size by examining the structure that was returned in particular how well the spiral arms were effected for the  $850\mu\text{m}$ , and how well the disk was preserved in the  $450\mu\text{m}$ . The spatial effect of the filters can be seen in figure 2.2 for the  $450\mu\text{m}$  and figure 2.2 for the  $850\mu\text{m}$ . The maps were returned from MAKEMAP in units of pW with a pixel size of  $2''$  by  $2''$  for both the  $450\mu\text{m}$  and  $850\mu\text{m}$ .

The finalized  $450\mu\text{m}$  image was then re-gridded down to a  $4''$  by  $4''$  pixel grid, and flux calibration values of 491000 and 4710 were applied to convert from pW to mJy/beam and mJy/square arcsecond respectively. The  $850\mu\text{m}$

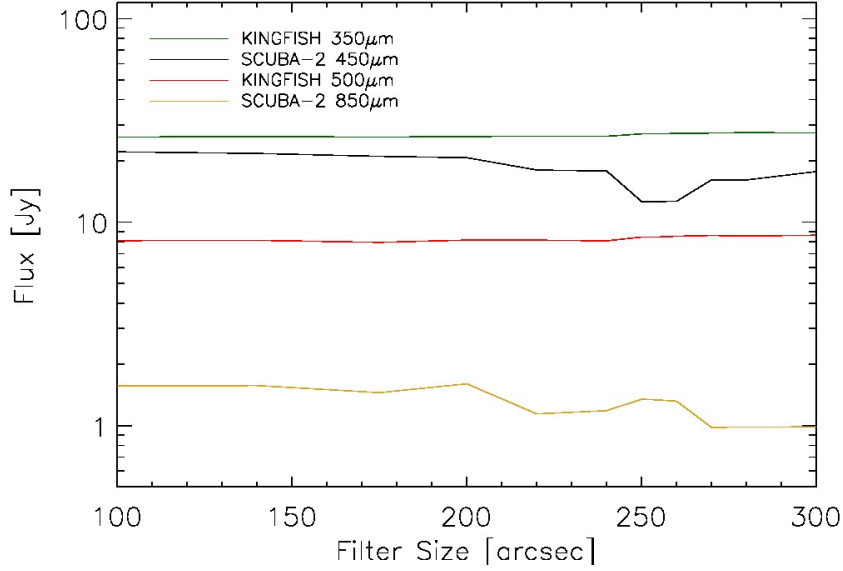


Figure 2.1 Returned flux values for NGC3627 with varying high-pass filter sizes.

Table 2.1. Properties of NGC3627 SCUBA-2 Observations

Observation	Beam Properties				RMS [mJy / Pixel]
	$\alpha$	$\theta_\alpha$	$\beta$	$\theta_\beta$	
450μm	$0.854 \pm 0.002$	$7.48'' \pm 0.03''$	$0.146 \pm 0.003$	$23.1'' \pm 0.2''$	3.42
850μm	$0.9624 \pm 0.0002$	$12.8'' \pm 0.004''$	$0.0376 \pm 0.0002$	$44.5'' \pm 0.09''$	0.476

maps were re-gridded to an  $8''$  by  $8''$  pixel size and used flux calibration values of 537000 and 2340 for mJy/beam and mJy/square arcsecond. The  $4''$  and  $8''$  pixels corresponded to a 180pc and 360pc size scale for our target, NGC3627. To simplify the analysis, the images are also converted to Jy/pixel. The 450μm and 850μm are shown in figures 2.2 and 2.2. The calibration values are determined from our calibrator source, Uranus. The overall noise in the final image can be seen in table 2.1.



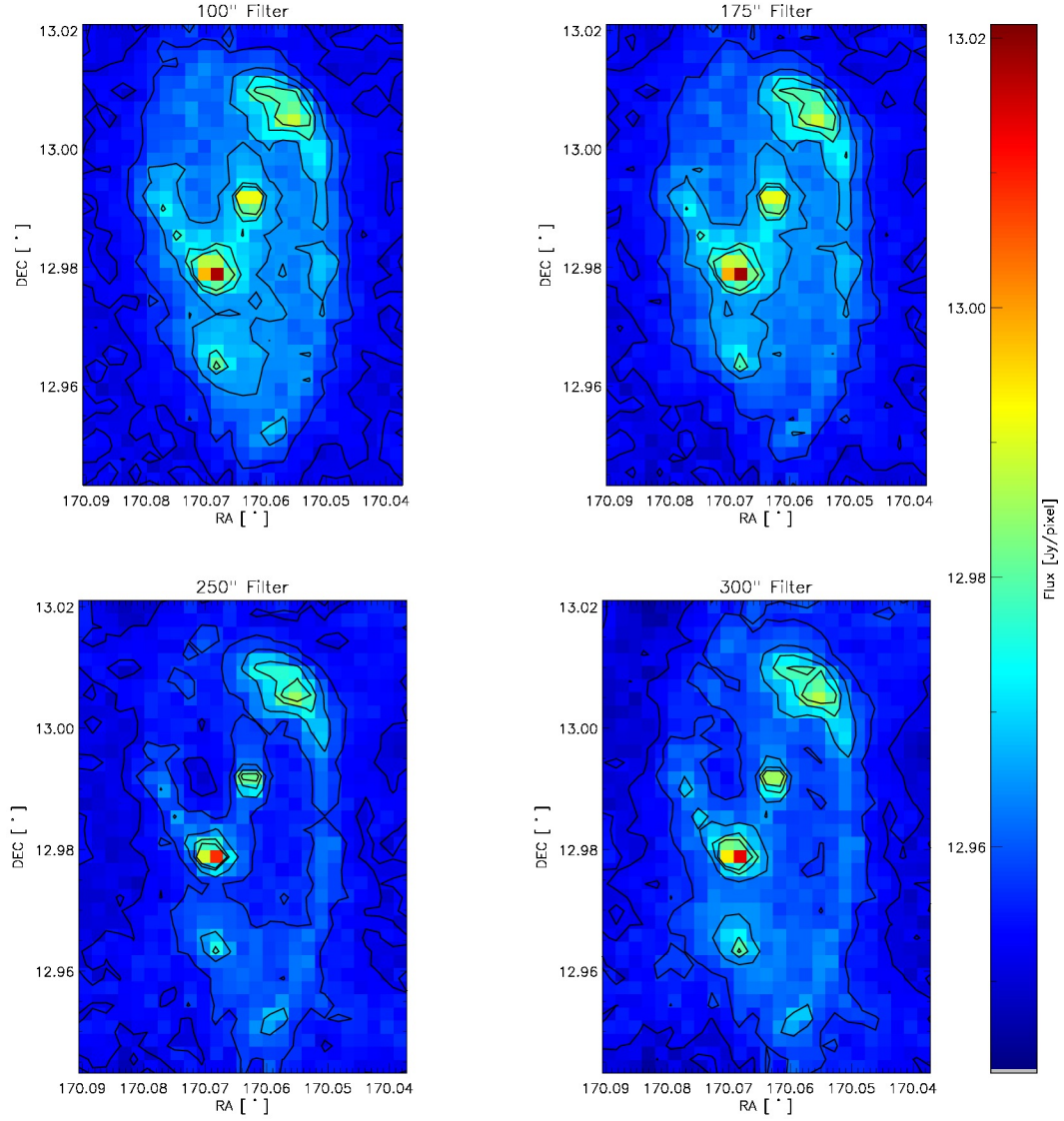


Figure 2.2 Four 450μm maps of NGC3627 using varying high-pass filter sizes. The contours shown are for 0.0, 0.02, 0.05, 0.08 and 0.1 Jy/pixel for each image.

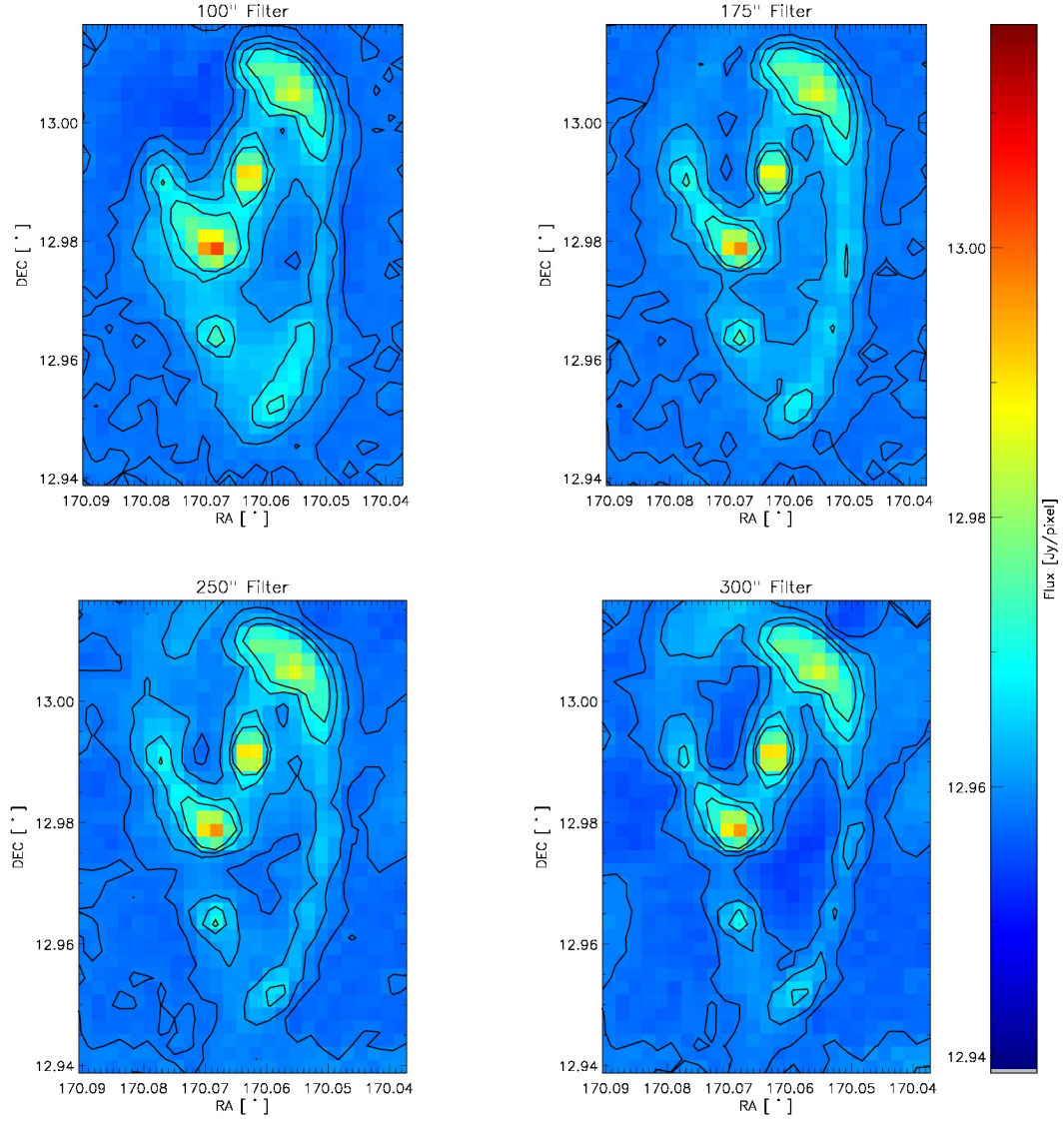


Figure 2.3 Four 850μm maps of NGC3627 using varying high-pass filter sizes. The contours shown are for 0.0, 0.002, 0.005, and 0.008 Jy/pixel for each image.

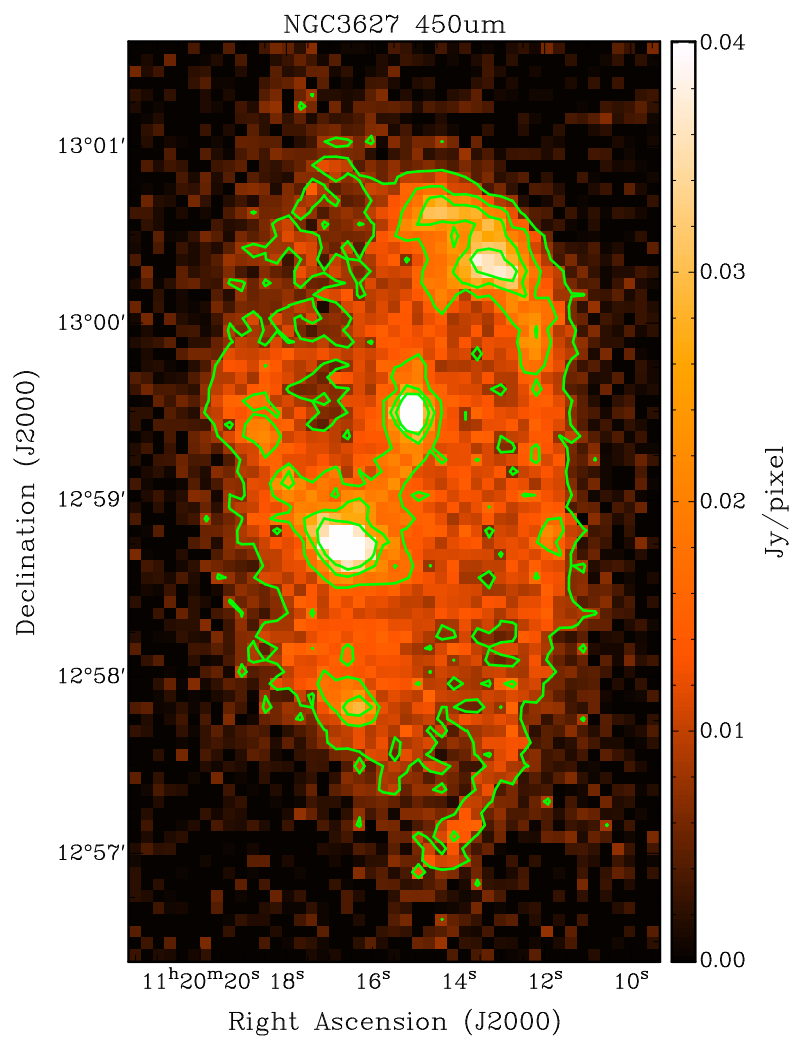


Figure 2.4 450 $\mu$ m observation produced at the end of the image production with 20%, 40%, 60%, and 80% contours.

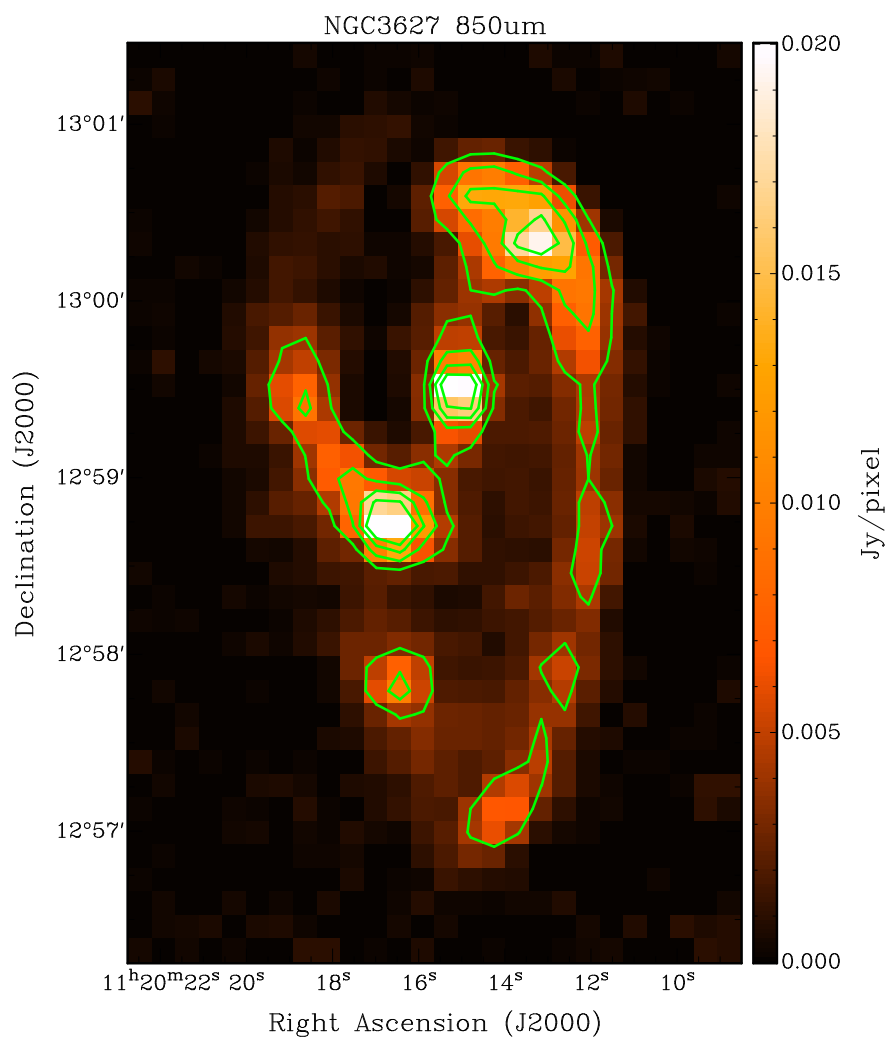


Figure 2.5 850 $\mu$ m observation produced at the end of the image production with 20%, 40%, 60%, and 80% contours.

### 2.2.1 Beam Shape of the $450\mu\text{m}$ and $850\mu\text{m}$ Data

The Uranus calibration images were also used in determining the shape of the beam for the  $450\mu\text{m}$  and  $850\mu\text{m}$  observations. The beam shape of both the  $450\mu\text{m}$  and  $850\mu\text{m}$  maps deviates from a single gaussian due to the second maximum of the airy diffraction pattern in the response function of the telescope and minor imperfections in the mirror of the JCMT due to boundaries of the panel Dempsey et al. (2013). This abnormality was best represented by a sum of two gaussians whose amplitude totals to unity (Dempsey et al., 2013). The average beam resolution for the  $450\mu\text{m}$  and  $850\mu\text{m}$  are reported in table 2.1 and match the values within uncertainty found in (Dempsey et al., 2013). The calibration images and beams can be seen in figure 2.2.1. The contribution of the error beam in the  $850\mu\text{m}$  emission is negligible and allows the beam to be approximated by a single gaussian. However, the contribution of the error beam in the  $450\mu\text{m}$  images was large enough to require special treatment in order to properly match beams for analysis.

## 2.3 Ancillary Data

The science goals of this thesis required data outside the capabilities of SCUBA-2. For instance, accurately determining the dust mass involved fitting the spectral energy distribution (SED) for NGC3627. To successfully fit an SED, we needed shorter wavelength data to fully probe the cold component of this galaxy. We used data ranging from  $100\mu\text{m}$  to  $500\mu\text{m}$  from the KINGFISH survey ((Kennicutt et al., 2011)) to gain a large enough wavelength range for fitting the cold component. Secondly, the bandpass of the  $850\mu\text{m}$  emisison

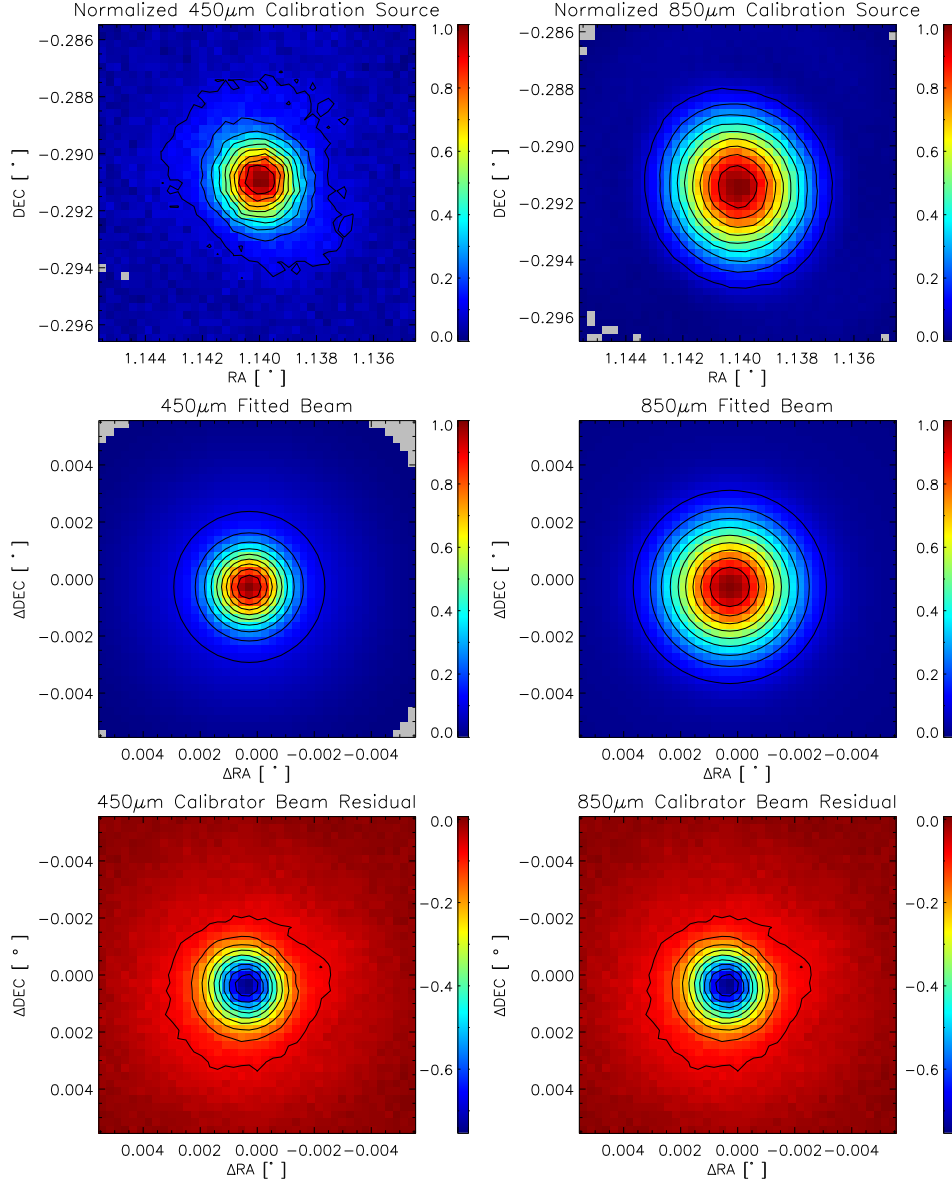


Figure 2.6 The top row shows the Uranus images taken on January, 5th 2012 for the 450 $\mu\text{m}$  on the left and the 850 $\mu\text{m}$  on the right. The bottom row shows the fitted beams for the 450 $\mu\text{m}$  on the right and 850 $\mu\text{m}$  on the left using the double gaussian beam shape. The contours in the image are from 10% to 90% in intervals of 10%.

contains the CO j=3-2 transmission line. In order to get a valid approximation on the dust mass, this contribution had to be removed. We used emission data from the NGLS using HARP instrumentation on the JCMT (Wilson et al., 2012). When a dust mass was obtained, we used CO j=1-0 from the Nobeyama 45-m telescope ((Kuno et al., 2007)), CO j=2-1 from HERACLES ((Leroy et al., 2009)), and *HI* observations from THINGS ((Walter et al., 2008)) to determine an reasonable molecular hydrogen mass to calculate a dust-to-gas ratio.

### 2.3.1 Key Insights on Nearby Galaxies: a Far-Infrared Survey with Herschel (KINGFISH)

The Key Insights on Nearby Galaxies: a Far-Infrared Survey with Herschel (KINGSFISH) was designed to be a follow up to the Spitzer Infrared Nearby Galaxies Survey (SINGS) (Kennicutt et al., 2003) with observations of the warm and cold component of dust emission using the increased resolution from Herschel (Kennicutt et al., 2011). The main science goals of the KINGFISH survey were to better understand the star formation processes that were shielded by dust, resolved studies of heating and cooling of the interstellar medium (ISM), and to build an inventory of how cold dust emission relates to other dust components in the ISM (Kennicutt et al., 2011). The survey consisted of studying 61 nearby galaxies ( $d < 30 \text{ Mpc}$ ) that cover a range of environments each observed at  $70 \mu\text{m}$ ,  $100 \mu\text{m}$ ,  $160 \mu\text{m}$ ,  $250 \mu\text{m}$ ,  $350 \mu\text{m}$ , and  $500 \mu\text{m}$ . Our analysis focuses on fitting the cold component of NGC3627's SED, so we omitted the  $70 \mu\text{m}$  emission from the fitting, and processed the

Table 2.2. Properties of NGC3627 KINGFISH Observations

Observation	Beam Properties $\theta_{beam}$	RMS $[Jy/Pixel]$	Percentage of Emission Removed
100 $\mu$ m	6.8''	2.24e-3	16.7%
160 $\mu$ m	11.6''	3.95e-3	18.8%
250 $\mu$ m	18.0''	2.47e-3	19.9%
350 $\mu$ m	24.9''	1.08e-3	21.8%
500 $\mu$ m	36.0''	3.87e-4	27.7%

data through MAKEMAP as described in § ???. The rms and beam size after the large scale structure has been removed can be seen in table 2.2, while the preconvolved maps are shown in figures 2.3.1 to 2.3.1.

### 2.3.2 Nearby Galaxy Legacy Survey (NGLS)

The Nearby Galaxy Legacy Survey is an HI-selected set of 155 galaxies contained in the annulus of  $2Mpc \leq r \leq 25Mpc$  using the instrumentation on the JCMT (Wilson et al., 2012). The NGLS consists of data observed in several wavelengths that include the 450 $\mu$ m and 850 $\mu$ m data used for this thesis. As mentioned previously, the bandpass for SCUBA-2's 850 $\mu$ m emission contains the CO j=3-2 line which is contained in the NGLS data set. We used the zeroth moment CO j=3-2 maps from the NGLS to determine the percentage of CO j=3-2 emission present in the 850 $\mu$ m band as well as removing it for an accurate SED analysis. The rms and resolution of the CO j=3-2 emission are shown in table 2.3, and the scan prior to convolution is shown in figure 2.3.2.



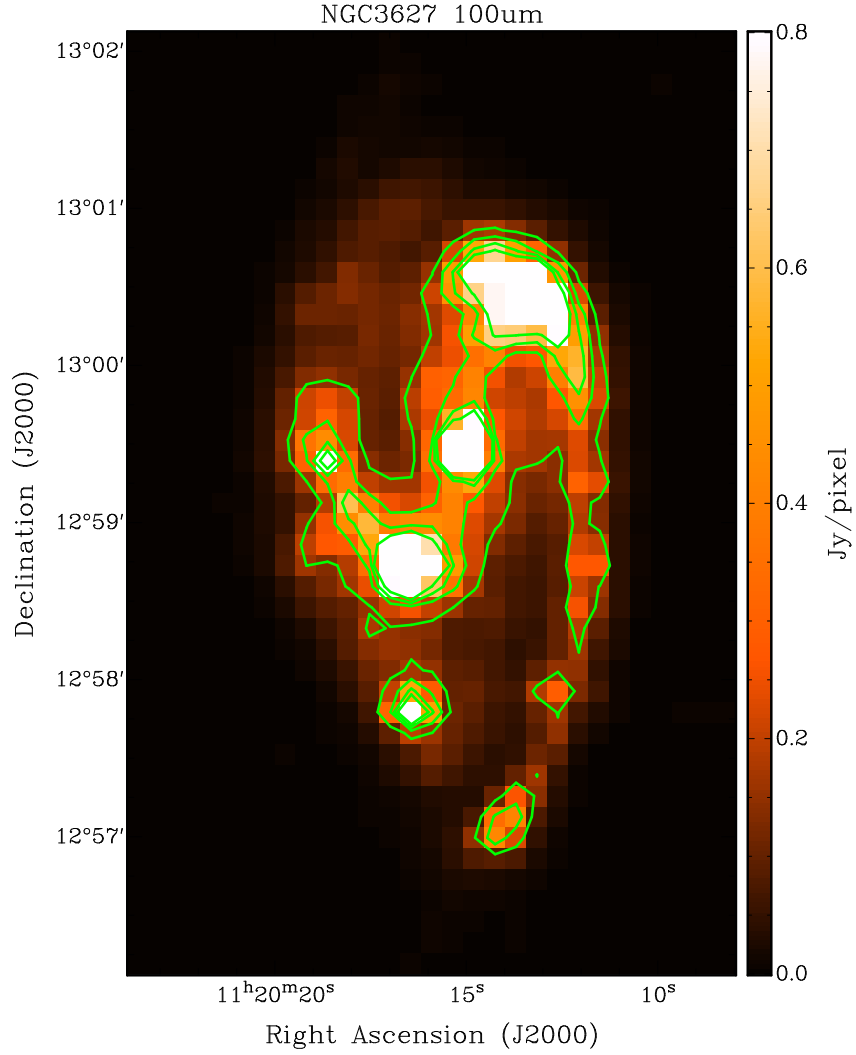


Figure 2.7 Residual of the MAKEMAP filtering of  $100\mu\text{m}$  observations with 20%, 40%, 60%, and 80% contours.

Table 2.3. Properties of NGC3627 NGLS Observations

Observation	Beam Properties $\theta_{beam}$	RMS $[Jy/Pixel]$	Percentage of Emission Removed
CO j=3-2	14.5''	1.28e-5	29.8%

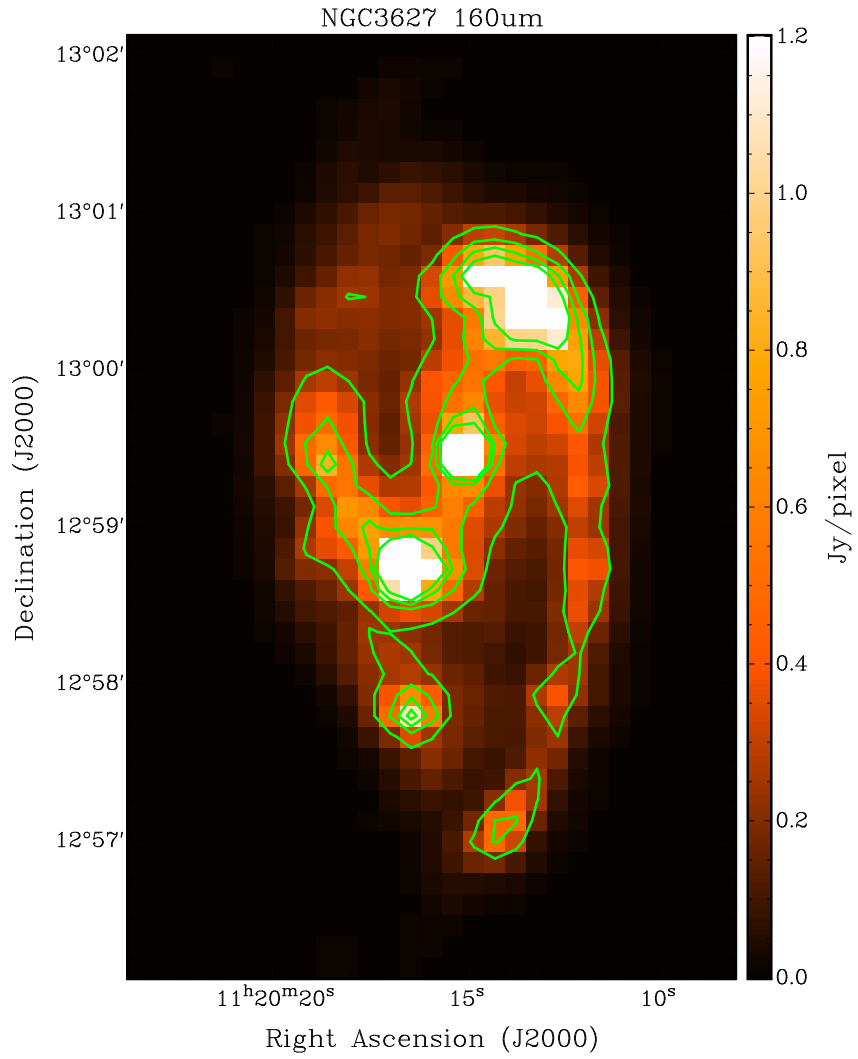


Figure 2.8 Residual of the MAKEMAP filtering of 160 $\mu$ m observations with 20%, 40%, 60%, and 80% contours.

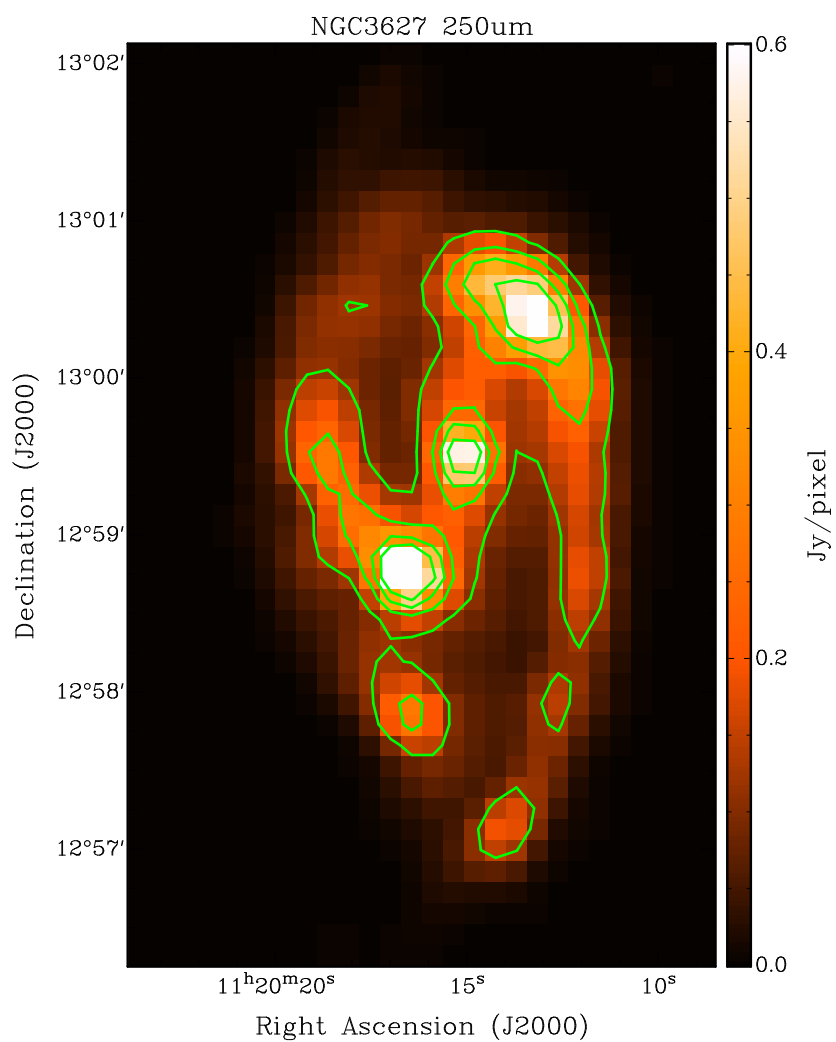


Figure 2.9 Residual of the MAKEMAP filtering of 250μm observations with 20%, 40%, 60%, and 80% contours.

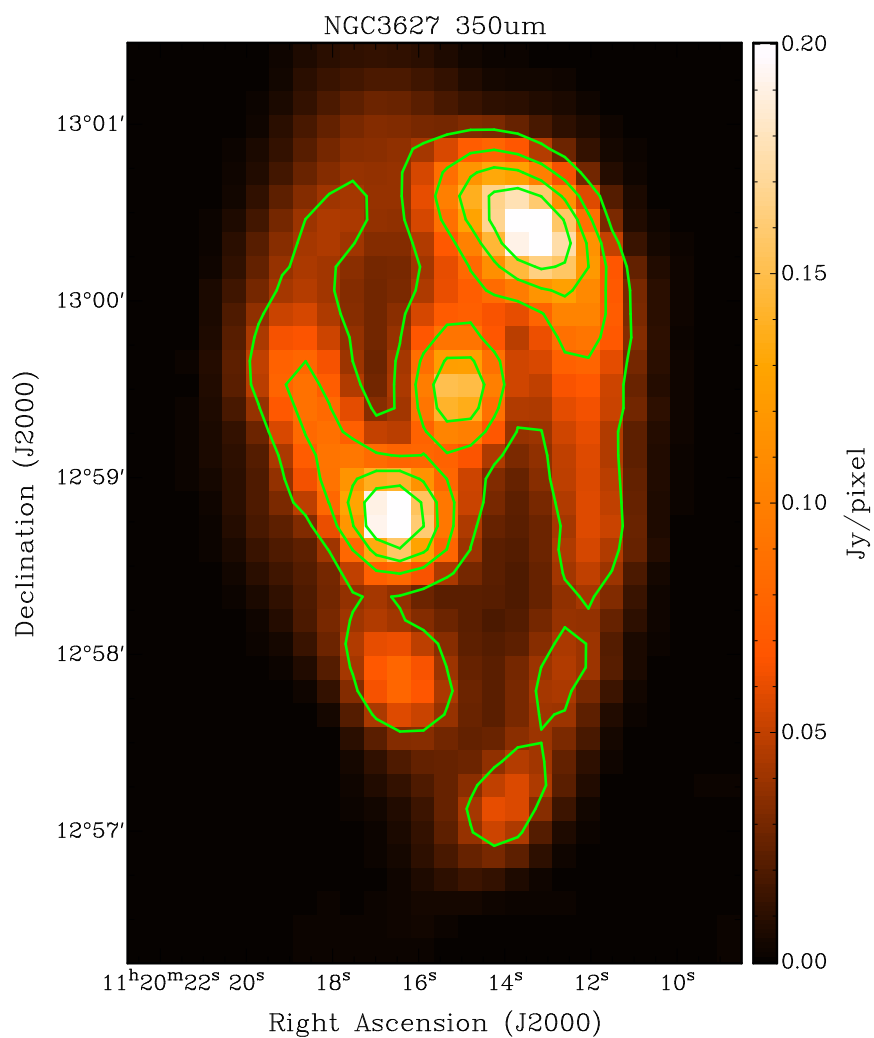


Figure 2.10 Residual of the MAKEMAP filtering of the  $350\mu\text{m}$  observations with 20%, 40%, 60%, and 80% contours.

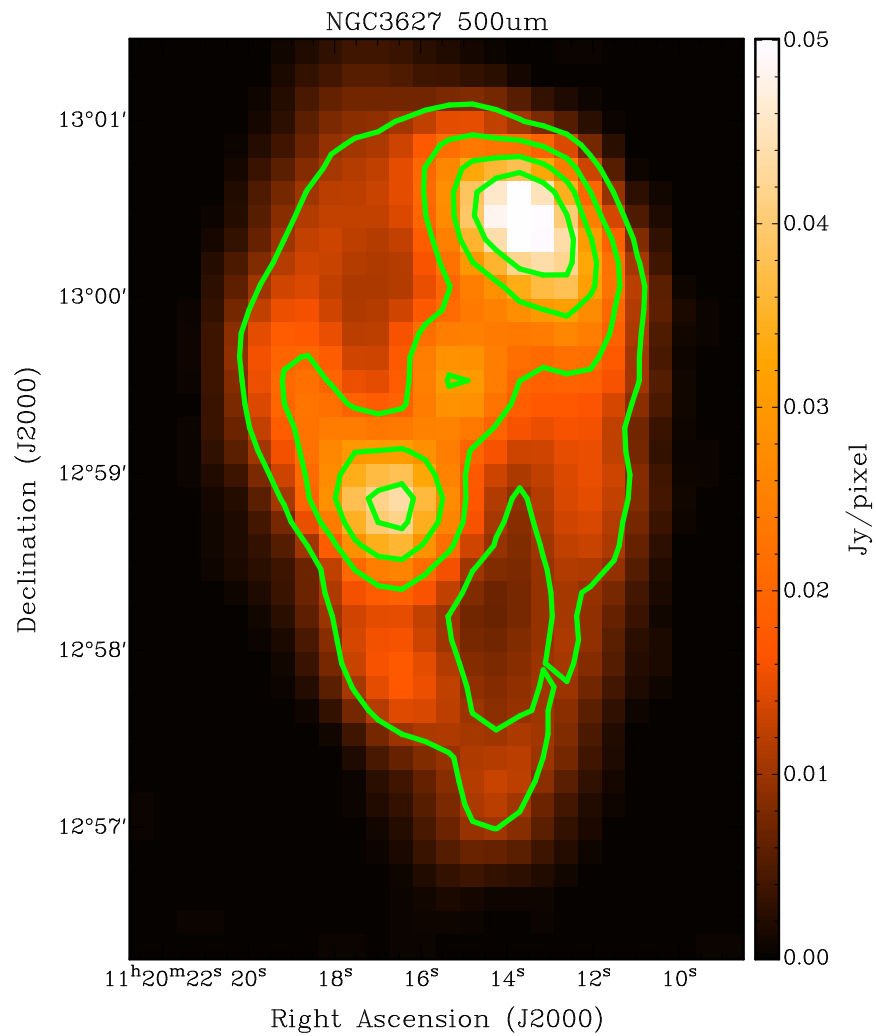


Figure 2.11 Residual of the MAKEMAP filtering of the 500 $\mu$ m observations with 20%, 40%, 60%, and 80% contours.

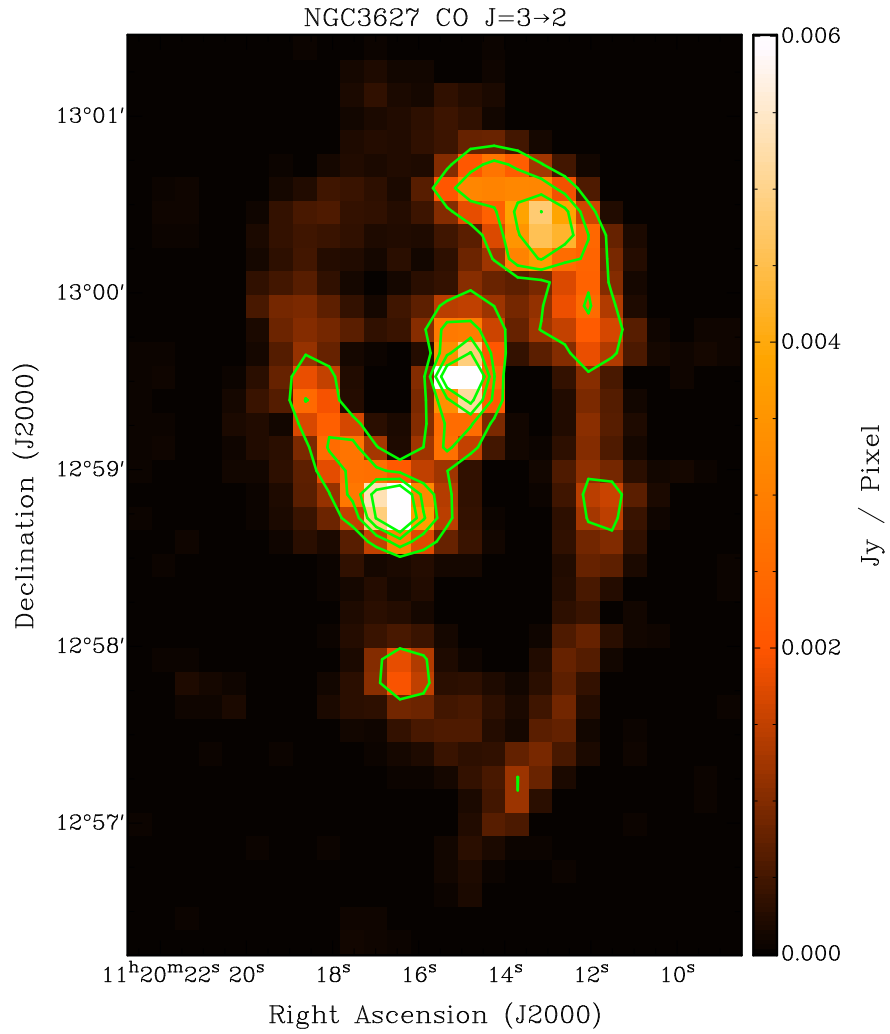


Figure 2.12 Residual of the MAKEMAP filtering of CO j=3-2 observations with 20%, 40%, 60%, and 80% contours.

Table 2.4. Properties of NGC3627 Nobeyama 45-m Observations

Observation	Beam Properties $\theta_{beam}$	RMS [K km/s]	Percentage of Emission Removed
CO j=1-0	15.0''	0.681	25.8%

### 2.3.3 Nobeyama 45-m

Determining a dust-to-gas ratio required the need for a molecular tracer to estimate the amount of molecular hydrogen present. The most frequently used tracer is CO j=1-0 due to its abundance in the ISM. The CO j=1-0 we used was taken from the Nobeyama 45-m CO Atlas of Nearby Spiral Galaxies observed to better understand the role of bars relating to molecular gas (Kuno et al., 2007). The Nobeyama 45-m CO Atlas consists of galaxies with morphologies ranging from Sa to Scd, located less than 25Mpc from the Milky Way, inclination values greater than  $79^\circ$ ,  $100\mu\text{m}$  flux greater than 10Jy, and spiral structure that has not been compromised through interactions. Any galaxies that met this criteria were then observed with the Nobeyama 45-m telescope (Kuno et al., 2007). The beam sizes and rms of the filtered CO j=1-0 map are displayed in table 2.4 and the final image product can be seen in figure 2.3.3.

### 2.3.4 Heterodyne Receiver Array CO-Line Extragalactic Survey (HERACLES)

The CO j=2-1 line was used to determine a  $2-1/1-0$  line ratio which can be used to trace a gradient in  $\alpha_{CO}$  and hint towards regions of high

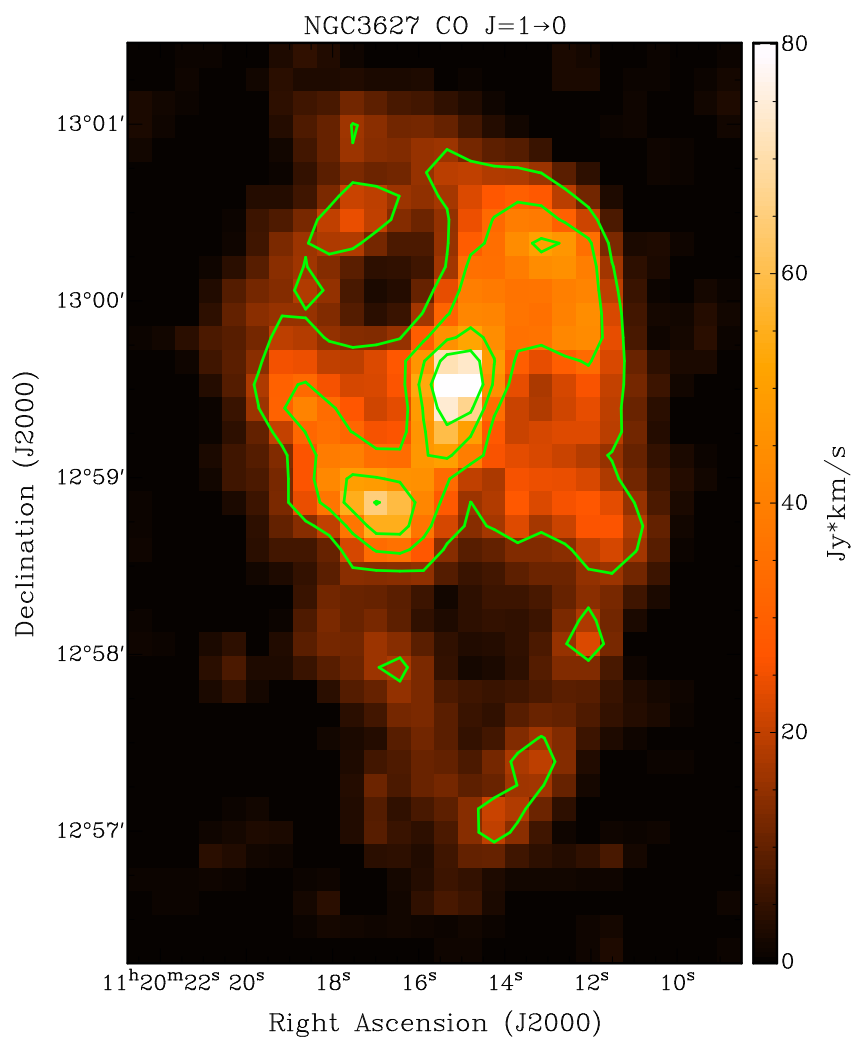


Figure 2.13 Residual of the MAKEMAP filtering of CO j=1-0 observations with 20%, 40%, 60%, and 80% contours.



Table 2.5. Properties of NGC3627 HERACLES Observations

Observation	Beam Properties $\theta_{beam}$	RMS [ $K\ km/s$ ]	Percentage of Emission Removed
CO j=2-1	13.0''	0.305	7.8%

star-formation (Reuter et al., 1996). We used the CO j=1-0 data from the Nobeyama 45-m telescope (§ 2.3.3), and CO j=2-1 from the Heterodyne Receiver Array CO-Line Extragalactic Survey (HERACLES) using the IRAM 30-m telescope. The main goal of HERACLES was to quantify the relationship between atomic and molecular gas and star formation using a large sample of galaxies ((Leroy et al., 2009)). The sample of galaxies chosen were targets contained in THINGS that were within observing limits of the IRAM 30-m telescope. The final image can be seen in figure 2.3.4 and the image properties can be seen in table 2.5.

### 2.3.5 The HI Nearby Galaxy Survey (THINGS)

To determine the gas to dust ratio we had to determine the total amount of gas present which required both atomic and molecular hydrogen. We approximated the amount of molecular hydrogen present by using CO j=1-0, and measured the amount of atomic hydrogen (HI) present. The source of our atomic hydrogen came from The HI Nearby Galaxy Survey (THINGS) designed to observe HI emission in nearby galaxies with the extreme spatial resolution of the Very Large Array (VLA). Targets in THINGS included many

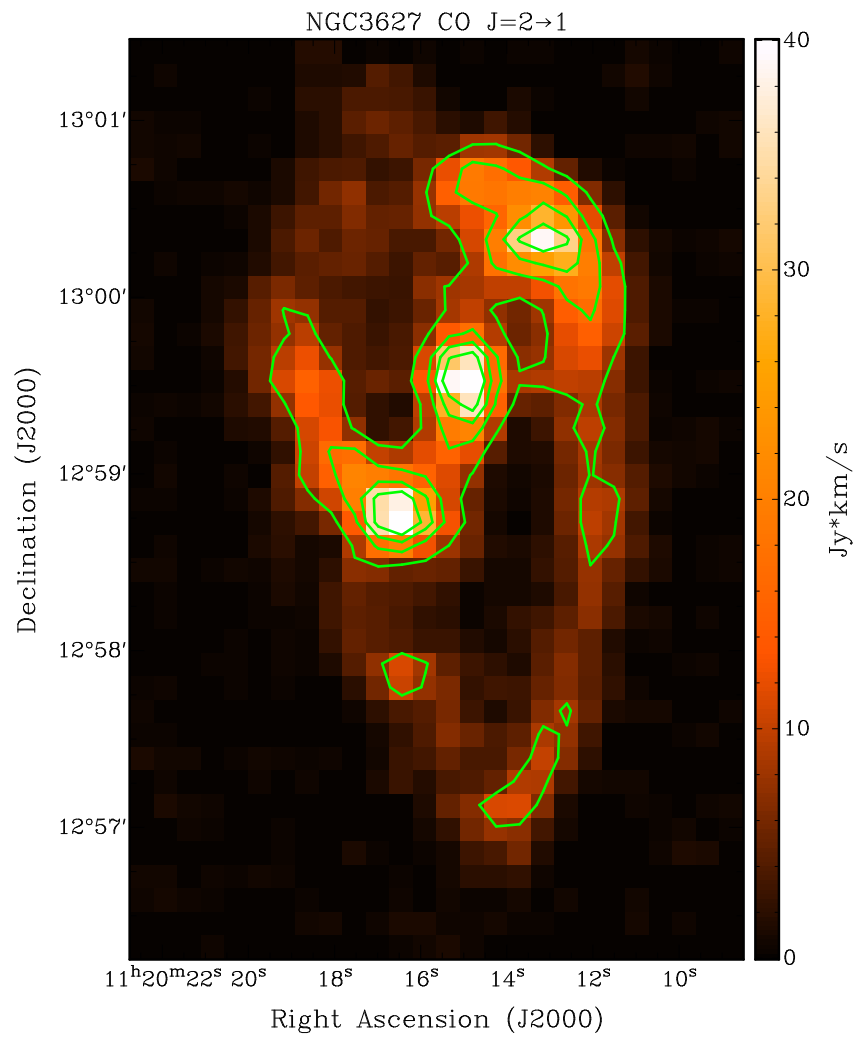


Figure 2.14 Residual of the MAKEMAP filtering of CO j=2-1 observations.

Table 2.6. Properties of NGC3627 THINGS Observations

Observation	Beam Properties			RMS	Percentage of Emission Removed
	$\theta_{maj}$	$\theta_{min}$	$\theta_{PA}$	$[M_{\odot}/pc^2]$	
HI	10.6''	8.85''	-48.0°	0.760	39.6%

of the SINGS targets with the exception of known HI poor sources (E/S0 type galaxies), dynamically complex systems (edge-on spirals), and large extended galaxies found in the local group (Walter et al., 2008). The resolution and rms of the filtered image are shown in table 2.6. The final data product is shown in figure 2.3.5.

## 2.4 Data Preparation for Analysis

Initially the data do not agree on several levels. The differences consist of the presence of the large scale structure in some but not all of our maps, different resolutions, and accounting for the beam shape of the  $450\mu\text{m}$ . We have taken several steps to correct these disagreements and maximize the compatibility of the data. In order to account for the varying beam resolutions, we use a gaussian convolution to increase the resolution of our maps to the largest beam size in our dataset,  $36''$ , using equation 2.2 to decide on an appropriate beam size such that  $\sigma_{desire}$  is the desired beam width,  $\sigma_{max}$  is the beam size we are convolving to, and  $\sigma_{given}$  is the beams size we are convolving from.

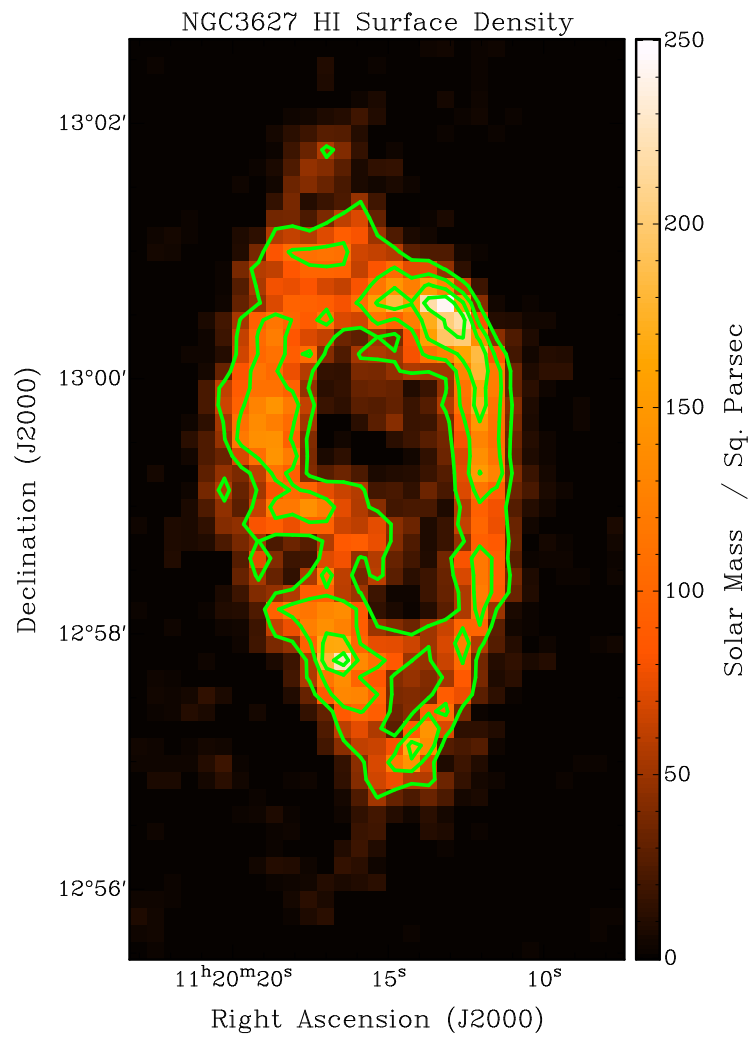


Figure 2.15 Residual of the MAKEMAP filtering of HI observations.

$$\sigma_{desire} = \sqrt{\sigma_{max}^2 - \sigma_{given}^2} \quad (2.2)$$

However, this only works when the beams are well approximated by a gaussian which is not the case for the  $450\mu\text{m}$  beam. The steps taken to match the resolution of the  $450\mu\text{m}$  beam with the rest of the data set is given in § 2.4.1. Removing any large scale structure from our ancillary data is implemented using a feature in MAKEMAP that allows us to add fake sources into the data during production. The fake source implementation allows us to remove the same amount of large scale structure from our ancillary data as was removed from the SCUBA-2 data. The steps taken to prepare the ancillary data are described in §2.4.2.

#### 2.4.1 Accounting for the $450\mu\text{m}$ Error Beam

Taking the  $450\mu\text{m}$  error beam into consideration is different than normal beam convolution in the sense that we are not convolving the higher resolution map to the lowest resolution. Instead we are adding in an error beams similar to the  $450\mu\text{m}$  observations to all of our observations. We have to take these steps because convolving a double gaussian beam with a single gaussian kernel will not sufficiently remove the error component of our beam resulting in a poor approximation to the wings of our beam shape.

In order to accommodate the  $450\mu\text{m}$  map's error beam, we used a method employed by another SCUBA-2 survey, the Gould-Belt Survey team. This method used the distributive nature of the Fourier transform to create similar

error components in the beam resolutions we were convolving to and from. Carrying out this convolution involved breaking the  $450\mu\text{m}$  beam into its two components,  $\sigma_\alpha$  and  $\sigma_\beta$  to represent the main beam and error beam. The lowest resolution beam shape,  $\sigma_{max}$  is convolved with the two components and the resulting beams are added together. This process produces an equivalent two component beam as the  $450\mu\text{m}$  beam convolved with  $\sigma_{max}$ . This relationship is shown in equation 2.3 where  $X_{max}$  is the beam width of the our lowest resolution,  $X_\alpha$  and  $X_\beta$  are the main and error beam of the  $450\mu\text{m}$  observations, and  $X_{450\mu\text{m}}$  is the double gaussian beam shape of the  $450\mu\text{m}$  observations.

$$X_{max} * X_\alpha + X_{max} * X_\beta = (X_\alpha + X_\beta) * X_{max} = X_{450\mu\text{m}} * X_{max} \quad (2.3)$$

#### 2.4.2 Extended Structure Removal via MAKEMAP

Due to the combination of methods used in MAKEMAP, large scale/extended structure is removed from the final SCUBA-2 images. However, in all of our ancillary data the large scale emission was present in the initial maps. The removal of the extended features from our support data was carried out by passing the data through MAKEMAP using a special function called fakesource. Implementing fakesource allows us to pass an image through processing and have it added into the image being processed. We use the  $850\mu\text{m}$  map as our base image for the fakesource process. The output image then consists of the added data map and the  $850\mu\text{m}$  map, and the ancillary data was then isolated by subtracting the  $850\mu\text{m}$  image from the fakesource image.

Preparing the data to be implemented consisted either converting the images from their native units into pW using the  $850\mu\text{m}$  flux calibration factor and scaled down to match the observed signal or by just applying a scaling factor. Which method is used is based on the desired units of the final map, and can be separated by what results the data is used to obtain.

The data used in the SED fitting (KINGFISH and NGLS) were scaled to pW so they could have as similar a reduction and calibration process as the SCUBA-2 maps. The KINGFISH data has the appropriate calibration factor applied to convert from either MJy/sr to pW in the case of the  $250\mu\text{m}$ ,  $350\mu\text{m}$ , and  $500\mu\text{m}$  or Jy/pixel to pW for the  $100\mu\text{m}$  and  $160\mu\text{m}$ . Converting the CO j=3-2 involved applying a scaling constant of  $0.70 [\text{mJy/beam}][\text{K km/s}]^{-1}$  (Drabek et al., 2012) prior to applying the  $850\mu\text{m}$  calibration factor to convert to pW. After the data has been converted to pW, the image used as a fakesource is then scaled down to the same order of magnitude as the base image. After the fakesource image has been processed and extracted, the maps are calibrated using the same values as the  $850\mu$  map and scaled to an  $8''$  by  $8''$  grid. The amount of extended flux lost in the KINGFISH and NGLS is shown in tables 2.2 and 2.3.

The rest of the ancillary data is used in calculating a dust to gas ratio, and follows nearly the same process as the SED data filtering. The major difference is the CO j=1-0, CO j=2-1 and HI maps need to remain in their original units of K km/s and  $\text{M}_{\odot}/\text{pc}^2$ . This necessity simplified the process by only requiring a scaling factor of 0.001 to be applied to the original maps. After the data is scaled, it is filtered using the fakesource option in MAKEMAP with the

850 $\mu$ m observation as the base image. The atomic and molecular gas maps were then isolated in the same fashion as the KINGFISH and NGLS, however they were rescaled back to their original values and fit to an 8'' by 8'' grid. The amount of emission lost is shown in tables 2.4, 2.5, and 2.6.



## Chapter 3

### Results

#### 3.1 Will they ever get here?

## Chapter 4

### Discussion

#### 4.1 Talk to the hand

## Chapter 5

## Conclusions

Sandstrom et al. (2013)

## Bibliography

- Abel, T., Anninos, P., Zhang, Y., & Norman, M. L. 1997, *New A*, 2, 181
- Chapin, E. L., Berry, D. S., Gibb, A. G., Jenness, T., Scott, D., Tilanus, R. P. J., Economou, F., & Holland, W. S. 2013, *MNRAS*, 430, 2545
- Dempsey, J. T., Friberg, P., Jenness, T., Tilanus, R. P. J., Thomas, H. S., Holland, W. S., Bintley, D., Berry, D. S., Chapin, E. L., Chrysostomou, A., Davis, G. R., Gibb, A. G., Parsons, H., & Robson, E. I. 2013, *MNRAS*, 430, 2534
- Dobbs, C. L., Krumholz, M. R., Ballesteros-Paredes, J., Bolatto, A. D., Fukui, Y., Heyer, M., Mac Low, M.-M., Ostriker, E. C., & Vázquez-Semadeni, E. 2013, *ArXiv e-prints*
- Drabek, E., Hatchell, J., Friberg, P., Richer, J., Graves, S., Buckle, J. V., Nutter, D., Johnstone, D., & Di Francesco, J. 2012, *MNRAS*, 426, 23
- Draine, B. T. 2011, *Physics of the Interstellar and Intergalactic Medium*
- Elmegreen, B. G. 1987, *ApJ*, 312, 626
- Field, G. B. & Saslaw, W. C. 1965, *ApJ*, 142, 568
- Glover, S. C. O. 2003, *ApJ*, 584, 331
- Gould, R. J. & Salpeter, E. E. 1963, *ApJ*, 138, 393

Gry, C., Boulanger, F., Nehmé, C., Pineau des Forêts, G., Habart, E., & Falgarone, E. 2002, *A&A*, 391, 675

Herbst, E., Chang, Q., & Cuppen, H. M. 2005, *Journal of Physics Conference Series*, 6, 18

Holland, W. S., Bintley, D., Chapin, E. L., Chrysostomou, A., Davis, G. R., Dempsey, J. T., Duncan, W. D., Fich, M., Friberg, P., Halpern, M., Irwin, K. D., Jenness, T., Kelly, B. D., MacIntosh, M. J., Robson, E. I., Scott, D., Ade, P. A. R., Atad-Ettdedgui, E., Berry, D. S., Craig, S. C., Gao, X., Gibb, A. G., Hilton, G. C., Hollister, M. I., Kycia, J. B., Lunney, D. W., McGregor, H., Montgomery, D., Parkes, W., Tilanus, R. P. J., Ullom, J. N., Walther, C. A., Walton, A. J., Woodcraft, A. L., Amiri, M., Atkinson, D., Burger, B., Chuter, T., Coulson, I. M., Doriese, W. B., Dunare, C., Economou, F., Niemack, M. D., Parsons, H. A. L., Reintsema, C. D., Sibthorpe, B., Smail, I., Sudiwala, R., & Thomas, H. S. 2013, *MNRAS*, 430, 2513

Jura, M. 1975, *ApJ*, 197, 575

Kennicutt, R. C., Calzetti, D., Aniano, G., Appleton, P., Armus, L., Beirão, P., Bolatto, A. D., Brandl, B., Crocker, A., Croxall, K., Dale, D. A., Meyer, J. D., Draine, B. T., Engelbracht, C. W., Galametz, M., Gordon, K. D., Groves, B., Hao, C.-N., Helou, G., Hinz, J., Hunt, L. K., Johnson, B., Koda, J., Krause, O., Leroy, A. K., Li, Y., Meidt, S., Montiel, E., Murphy, E. J., Rahman, N., Rix, H.-W., Roussel, H., Sandstrom, K., Sauvage, M., Schinnerer, E., Skibba, R., Smith, J. D. T., Srinivasan, S., Vigroux, L., Walter, F., Wilson, C. D., Wolfire, M., & Zibetti, S. 2011, *PASP*, 123, 1347

Kennicutt, R. C. & Evans, N. J. 2012, *ARA&A*, 50, 531

Kennicutt, Jr., R. C., Armus, L., Bendo, G., Calzetti, D., Dale, D. A., Draine, B. T., Engelbracht, C. W., Gordon, K. D., Grauer, A. D., Helou, G., Hollenbach, D. J., Jarrett, T. H., Kewley, L. J., Leitherer, C., Li, A., Malhotra, S., Regan, M. W., Rieke, G. H., Rieke, M. J., Roussel, H., Smith, J.-D. T., Thornley, M. D., & Walter, F. 2003, *PASP*, 115, 928

Kim, W.-T. & Ostriker, E. C. 2001, *ApJ*, 559, 70

Krumholz, M. R. 2014, ArXiv e-prints

Kuno, N., Sato, N., Nakanishi, H., Hirota, A., Tosaki, T., Shioya, Y., Sorai, K., Nakai, N., Nishiyama, K., & Vila-Vilaró, B. 2007, *PASJ*, 59, 117

Kwan, J. 1979, *ApJ*, 229, 567

Leroy, A. K., Walter, F., Bigiel, F., Usero, A., Weiss, A., Brinks, E., de Blok, W. J. G., Kennicutt, R. C., Schuster, K.-F., Kramer, C., Wiesenmeyer, H. W., & Roussel, H. 2009, *AJ*, 137, 4670

McKee, C. F. & Ostriker, E. C. 2007, *ARA&A*, 45, 565

Palla, F., Salpeter, E. E., & Stahler, S. W. 1983, *ApJ*, 271, 632

Parker, E. N. 1966, *ApJ*, 145, 811

Pirronello, V., Liu, C., Shen, L., & Vidali, G. 1997, *ApJ*, 475, L69

Reuter, H.-P., Sievers, A. W., Pohl, M., Lesch, H., & Wielebinski, R. 1996, *A&A*, 306, 721

Sandstrom, K. M., Leroy, A. K., Walter, F., Bolatto, A. D., Croxall, K. V., Draine, B. T., Wilson, C. D., Wolfire, M., Calzetti, D., Kennicutt, R. C., Aniano, G., Donovan Meyer, J., Usero, A., Bigiel, F., Brinks, E., de Blok, W. J. G., Crocker, A., Dale, D., Engelbracht, C. W., Galametz, M., Groves, B., Hunt, L. K., Koda, J., Kreckel, K., Linz, H., Meidt, S., Pellegrini, E., Rix, H.-W., Roussel, H., Schinnerer, E., Schruba, A., Schuster, K.-F., Skibba, R., van der Laan, T., Appleton, P., Armus, L., Brandl, B., Gordon, K., Hinz, J., Krause, O., Montiel, E., Sauvage, M., Schmiedeke, A., Smith, J. D. T., & Vigroux, L. 2013, *ApJ*, 777, 5

Walter, F., Brinks, E., de Blok, W. J. G., Bigiel, F., Kennicutt, Jr., R. C., Thornley, M. D., & Leroy, A. 2008, *AJ*, 136, 2563

Wilson, C. D., Warren, B. E., Israel, F. P., Serjeant, S., Attewell, D., Bendo, G. J., Butner, H. M., Chanial, P., Clements, D. L., Golding, J., Heesen, V., Irwin, J., Leech, J., Matthews, H. E., Mühle, S., Mortier, A. M. J., Petitpas, G., Sánchez-Gallego, J. R., Sinukoff, E., Shorten, K., Tan, B. K., Tilanus, R. P. J., Usero, A., Vaccari, M., Wiegert, T., Zhu, M., Alexander, D. M., Alexander, P., Azimlu, M., Barmby, P., Brar, R., Bridge, C., Brinks, E., Brooks, S., Coppin, K., Côté, S., Côté, P., Courteau, S., Davies, J., Eales, S., Fich, M., Hudson, M., Hughes, D. H., Ivison, R. J., Knapen, J. H., Page, M., Parkin, T. J., Rigopoulou, D., Rosolowsky, E., Seaquist, E. R., Spekkens, K., Tanvir, N., van der Hulst, J. M., van der Werf, P., Vlahakis, C., Webb, T. M., Weferling, B., & White, G. J. 2012, *MNRAS*, 424, 3050

Wolfire, M. G., McKee, C. F., Hollenbach, D., & Tielens, A. G. G. M. 2003, *ApJ*, 587, 278

**M.Sc. Thesis — Jonathan H. Newton — McMaster University - Physics and Astronomy — 2014**

Wolfire, M. G., Tielens, A. G. G. M., Hollenbach, D., & Kaufman, M. J. 2008,  
ApJ, 680, 384